

Chemical Targeting of the ATXN1 aa99–163 Interaction Site Suppresses polyQ-Expanded Protein Dimerization

Ioannis Gkekas,[#] Katerina Pliatsika,[#] Stelios Mylonas, Sotirios Katsamakas, Apostolos Axenopoulos, Simona Kostova, Erich E. Wanker, Dimitra Hadjipavlou-Litina, Konstantinos Xanthopoulos, Petros Daras, and Spyros Petrakis*



Cite This: <https://doi.org/10.1021/acsomega.5c02465>



Read Online

ACCESS |



Metrics & More

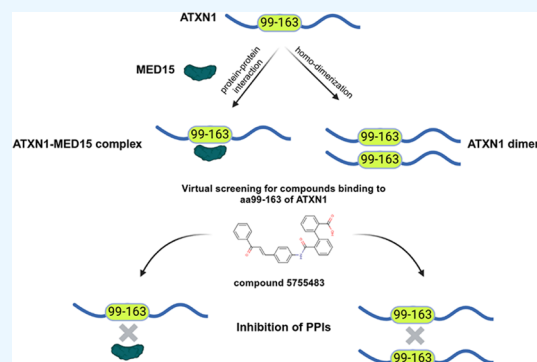


Article Recommendations



Supporting Information

ABSTRACT: Spinocerebellar ataxia type 1 (SCA1) is a neurodegenerative disease caused by the expansion of a polyglutamine (polyQ) tract in the ATXN1 protein. This expansion is thought to be responsible for the gradual aggregation of the mutant protein, which is associated with increased cytotoxicity and neuronal cell death. Apart from the polyQ tract, other domains in ATXN1 are also involved in the initial events of protein aggregation, such as a dimerization domain that promotes protein oligomerization. ATXN1 interacts with various proteins; among them, MED15 significantly enhances the aggregation of the polyQ-expanded protein. Therefore, we set to identify the interaction site between ATXN1 and MED15 and assess whether its chemical targeting would affect polyQ protein aggregation. First, we predicted the structures of ATXN1 and MED15 and simulated their interaction. We experimentally validated that amino acids (aa) 99–163 of ATXN1 and aa548–665 of MED15 are critical for this protein–protein interaction (PPI). We also showed that the aa99–163 domain in ATXN1 is involved in the dimerization of the mutant isoform. Targeting this domain with a chemical compound identified through virtual screening (Chembridge ID: 5755483) inhibited both the interaction of ATXN1 with MED15 and the dimerization of polyQ-expanded ATXN1. These results strengthen our assumption that the aa99–163 domain of ATXN1 may be involved in polyQ protein aggregation and highlight compound 5755483 as a potent first-in-class therapeutic agent for SCA1.



INTRODUCTION

Spinocerebellar ataxia type 1 (SCA1) is an autosomal dominant, progressive, and fatal neurodegenerative disease. It is caused by the expansion of CAG trinucleotide repeats in the *ATXN1* gene, which encodes polyglutamine (polyQ) residues in the relevant ataxin-1 (ATXN1) protein. Mutant ATXN1 exhibits a characteristic propensity for the formation of intranuclear inclusion bodies (IIBs) within affected neurons of SCA1 patients.^{1,2} Although *ATXN1* is broadly expressed in the brain, cerebellar Purkinje cells display selective neurodegeneration, which is associated with the ataxic phenotype in SCA1.³ However, in recent years, it has become evident that other brain regions, such as the brainstem, cerebral cortex, and striatum are also affected in SCA1.^{4,5}

ATXN1 contains multiple domains, each of which plays a crucial role in diverse subcellular functions. Located at the N-terminal region, the polyQ tract (aa197–225) is necessary for disease development.^{6,7} Beyond the polyQ tract, other regions significantly contribute to the aggregation process. For example, the AXH domain promotes oligomerization, contributing to the aggregation of mutant ATXN1. Computational analysis indicates that deletion or replacement of the AXH

domain reduces the aggregation propensity of ATXN1.^{8,9} Additionally, both the self-association region (SAR, residues 494–604) and the C-terminal region (residues 690–816) are implicated in the self-interaction and aggregation of ATXN1. Moreover, the nuclear localization signal (NLS, residues 794–797) is a major determinant of nucleocytoplasmic shuttling of ATXN1, and mutations in the NLS abolish toxicity in a transgenic model of SCA1.¹⁰ These findings indicate that various domains within ATXN1 may affect its aggregation and potentially disease progression.

ATXN1 is involved in numerous protein–protein interactions (PPIs). Partners include the transcription factors Senseless/Gfi-1 and Sp1, the mediator of retinoid and thyroid hormone receptors SMRT/SMRTER, the polyQ binding protein-1 (PQBP1), the RNA splicing factor U2AF65, the

Received: March 17, 2025

Revised: June 4, 2025

Accepted: June 11, 2025

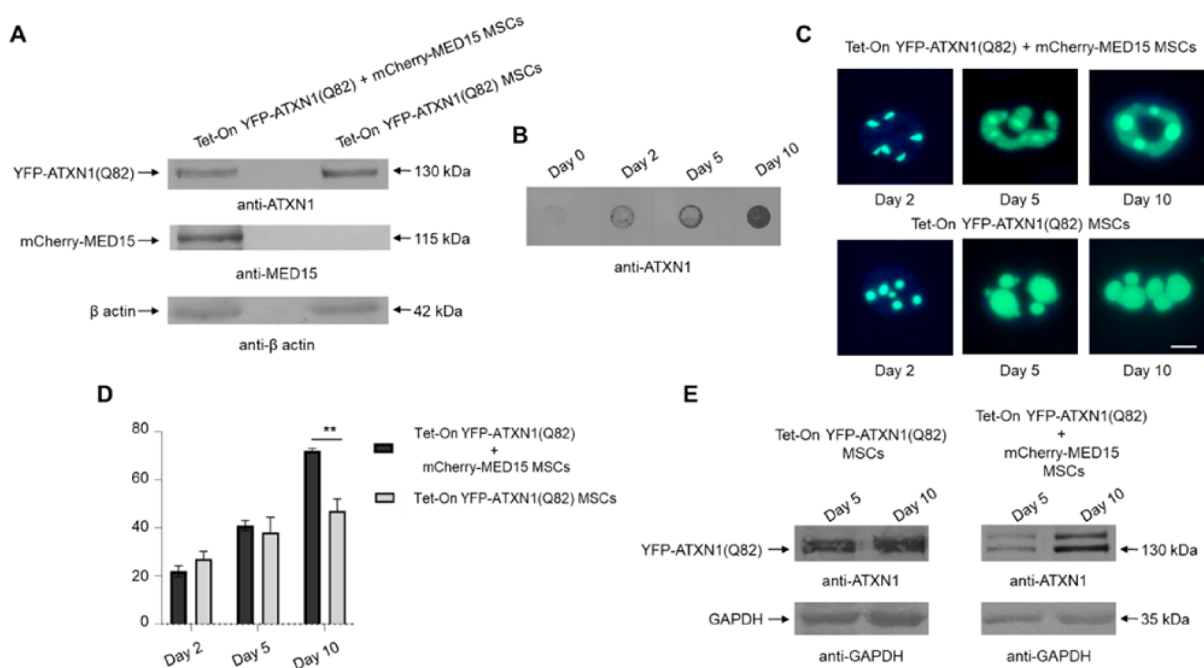


Figure 1. Effect of MED15 on the formation of ATXN1(Q82) IIBs. (A) Immunoblots for YFP-ATXN1(Q82) and mCherry-MED15 proteins in cell extracts of genetically modified MSCs. β -actin was used as a loading control. (B) Filter retardation assay for the detection of insoluble YFP-ATXN1(Q82) IIBs in extracts from Tet-On YFP-ATXN1(Q82) and mCherry-MED15 MSCs. (C) Morphological analysis of YFP-ATXN1(Q82) IIBs at different time points in the presence (top row) or absence (bottom row) of the mCherry-MED15 protein. Scale bar: 10 μ M. (D) Bar graph showing the average size of YFP-ATXN1(Q82) inclusion bodies (IIBs) in MSCs, analyzed using AggreCount software. The black bars represent cells co-producing YFP-ATXN1(Q82) and mCherry-MED15 proteins, while the gray bars indicate cells producing only YFP-ATXN1(Q82). (E) Immunoblot for soluble YFP-ATXN1(Q82) protein at D5 and D10 post induction. GAPDH was used as a loading control.

protein kinase A (PKA), and the transcriptional activator RAR-related orphan receptor alpha ($ROR\alpha$).^{11–15} The interaction between ATXN1 and the transcriptional repressor Capicua (CIC) has been extensively studied.¹⁶ This interaction affects cerebellar Purkinje cell pathogenesis, and mutations of key residues that suppress the interaction also reduce toxicity in a Purkinje cell-specific SCA1 mouse model.¹⁷ Furthermore, interactors may modulate the aggregation and proteotoxicity of the mutant ATXN1(Q82) protein. Notably, MED15, a subunit of the Mediator complex¹⁸ was previously shown to enhance ATXN1 cytotoxicity and protein aggregation¹⁹ potentially through coiled-coil (CC) interactions.²⁰

In this study, we aimed to identify the PPI site between ATXN1 and MED15 and investigate its involvement in the aggregation of polyQ-expanded ATXN1. Using computational and experimental methods, we showed that ATXN1 interacts with MED15 through an N-terminal domain (aa99–163) located upstream of the polyQ region. This domain is also important for ATXN1 dimerization. Targeting this domain with a chemical compound predicted through virtual screening significantly suppresses the interaction of ATXN1 with MED15 and the dimerization of the polyQ-expanded isoform.

RESULTS

The Aggregation of ATXN1(Q82) is Affected by MED15. Experimental evidence indicates that various domains within polyQ-expanded ATXN1 may affect its aggregation. For example, the AXH domain (residues 562–693) is essential for its dimerization, contributing to SCA1 pathology.^{8,9} Therefore, we first assessed the effect of this domain on ATXN1 protein dimerization. A cDNA clone of ATXN1 lacking the AXH domain (Δ AXH) was generated and used for the construction

of mCitrine-and NL-tagged LuTHy expression vectors.²¹ Compared to full-length (FL) ATXN1, which efficiently formed protein dimers, deletion of the AXH domain moderately suppressed protein dimerization of both the Q30 and Q82 isoforms (36% and 27%, respectively) in LuTHy assays (Figure S1A,B). These results indicate that the AXH domain weakly affects ATXN1 dimerization, which is the initial step in the polyQ-mediated aggregation process in SCA1. They also suggest that other domains in ATXN1 are involved in its dimerization and aggregation.

We previously showed that CC-rich protein MED15 interacts with the mutant isoform of ATXN1 and enhances its pathogenicity. This effect may be due to the expansion of CC regions adjacent to the N-terminus of the polyQ domain.²⁰ MED15 induces ATXN1(Q82) aggregation and co-localizes with polyQ IIBs in neuroblastoma cells.¹⁹ Here, we studied the impact of MED15 in a primary cell model of ATXN1(Q82) protein aggregation with no measurable cytotoxicity.²² mCherry-MED15 was stably overexpressed in MSCs inducibly co-expressing YFP-ATXN1(Q82), and the production of recombinant proteins was validated by SDS-PAGE and immunoblotting. YFP-ATXN1(Q82) was detected at the expected molecular weight of 130 kDa, while the mCherry-MED15 protein was detectable at the appropriate molecular weight (115 kDa) only in Tet-On YFP-ATXN1(Q82) + mCherry-MED15 cells (Figure 1A). Tet-On YFP-ATXN1(Q82) + mCherry-MED15 cells also accumulated insoluble polyQ IIBs, as confirmed by a filter retardation assay (Figure 1B). Next, we investigated the morphology of YFP-ATXN1(Q82) IIBs in the presence or absence of mCherry-MED15. To this end, MSCs were induced to produce the polyQ-expanded ATXN1 and imaged using fluorescence microscopy

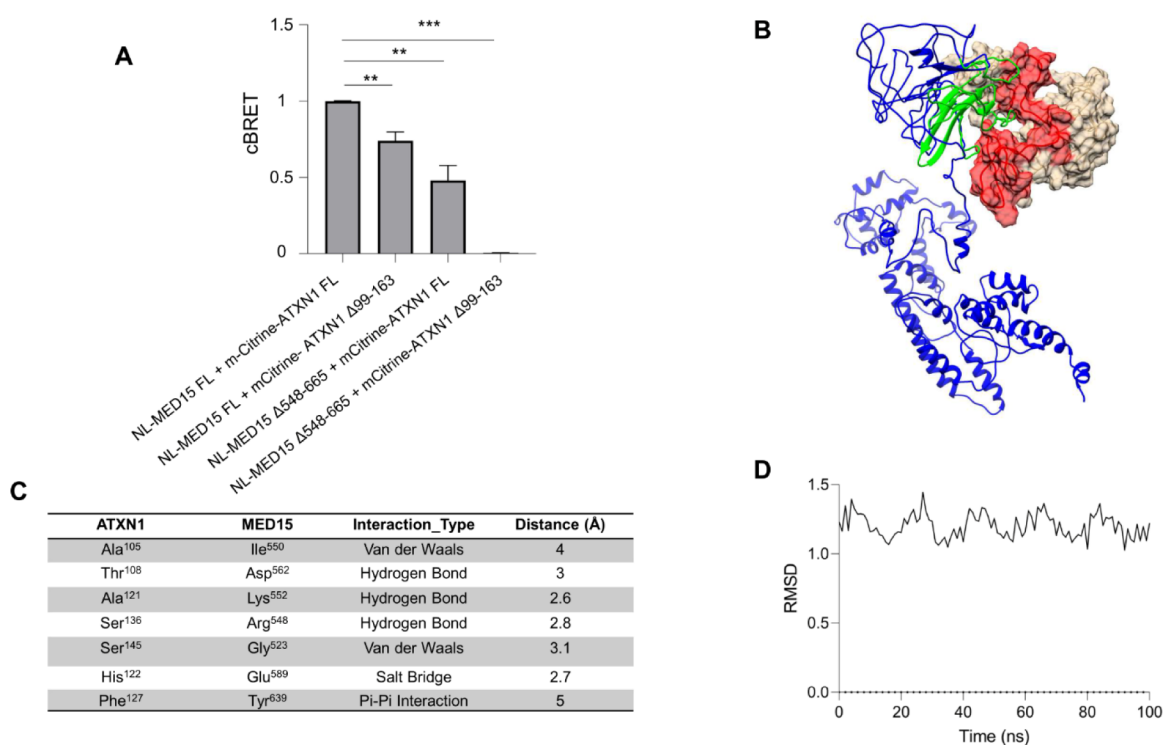


Figure 2. ATXN1 aa99–163 interacts with MED15 aa548–665. (A) LuThy assay for the quantification of the interaction between full-length ATXN1 and MED15 or deletion-carrying proteins (ATXN1 Δ99–163 or MED15 Δ548–665). The simultaneous deletion of both domains from the interacting proteins abolishes ATXN1-MED15 PPI. Error bars denote mean ± SD (* p value < 0.05, ** p < 0.01). (B) *In silico* docking of ATXN1^{NT} and MED15 mediated through aa99–163 (red) in ATXN1 and aa548–665 in MED15 (green). The ATXN1^{NT} protein is shown in white, while the MED15 protein is shown in blue, with the interaction domains highlighted. (C) Table summarizing the key residues mediating the ATXN1-MED15 PPI. It includes interacting residues in ATXN1 aa99–163 and MED15 aa548–665, along with the type of interaction and their respective distances (in Angstrom). (D) RMSD of the ATXN1-MED15 complex over the simulation time.

2, 5, and 10 days post induction. Distinct morphological differences in ATXN1 IIBs were observed. At day 2, IIBs in cells co-expressing both transgenes were irregular in shape compared to the spherical IIBs in MSCs expressing only YFP-ATXN1(Q82). By day 10, IIBs seemed to fuse and grow in size (Figures 1C,D and S2A). Immunoblots of cell extracts at day 5 and day 10 indicated a doublet band at approximately 130 kDa corresponding to YFP-ATXN1(Q82), which partially shifted toward a higher molecular weight band only in cells co-expressing *mCherry-MED15* (Figures 1E and S2B). This doublet band does not stain for MED15, excluding the possibility that it represents a YFP-ATXN1(Q82)-MED15 dimer (data not shown). Instead, the upper band may correspond to aggregation-prone YFP-ATXN1(Q82) protein molecules with a higher proportion of β sheets, which are known to migrate atypically in SDS-PAGE.²³ Taken together, these observations suggest that the aggregation of mutant ATXN1 is directly affected by its interacting partner MED15, as described previously.¹⁹

ATXN1 Interacts with MED15 through its aa99–163 Domain. We hypothesized that MED15 exerts its effect on ATXN1(Q82) aggregation through a direct PPI. The interaction between ATXN1-MED15 has been previously validated, along with the presence of MED15 in polyQ IIBs.¹⁹ To identify potential interaction sites, we simulated the ATXN1-MED15 PPI *in silico*. In the absence of crystallographic data, the I-TASSER software suite^{24,25} was utilized for a predictive modeling of the 3D structures of FL wild-type ATXN1 and MED15. Given the flexibility of the polyQ region in ATXN1, which complicates structural determination, we

also predicted the structures of ATXN1^{NT} and ATXN1^{CT}, corresponding to protein fragments upstream and downstream of the polyQ tract, respectively (Figure S3). Then, the predicted structures of ATXN1 (ATXN1 FL, ATXN1^{NT}, or ATXN1^{CT}) were individually docked with two models of MED15 having the highest C-score. The most promising docking complexes were selected based on the score and reproducibility of docking solutions. Following docking simulations, a list of potential interaction sites between MED15 and ATXN1, ATXN1^{NT}, or ATXN1^{CT} was generated. For example, ATXN1 aa99–163 was identified as an interaction site between ATXN1^{NT} and MED15 FL (Table S1).

The modeling capacity of protein prediction tools, including the recently developed AlphaFold, is strongly influenced by the presence of high-complexity domains in simulated proteins. This increases the possibility of low-confidence predictions.²⁶ Thus, we sought to assess whether ATXN1 interacts with MED15 through the predicted PPI sites. First, a LuThy assay was established to quantify the already known ATXN1-MED15 PPI. Expression clones of mCitrine-ATXN1 and NL-MED15 were generated and used for the transfection of HEK293T cells. Control experiments were conducted using mCitrine-NL or combinations of mCitrine-ATXN1/NL and mCitrine/NL-MED15 plasmids. BRET measurements of control PA-NL were performed to correct for donor luminescence bleed-through. Cells producing mCitrine-ATXN1/NL-MED15 recombinant proteins exhibited a significantly higher BRET ratio compared to control interactions,

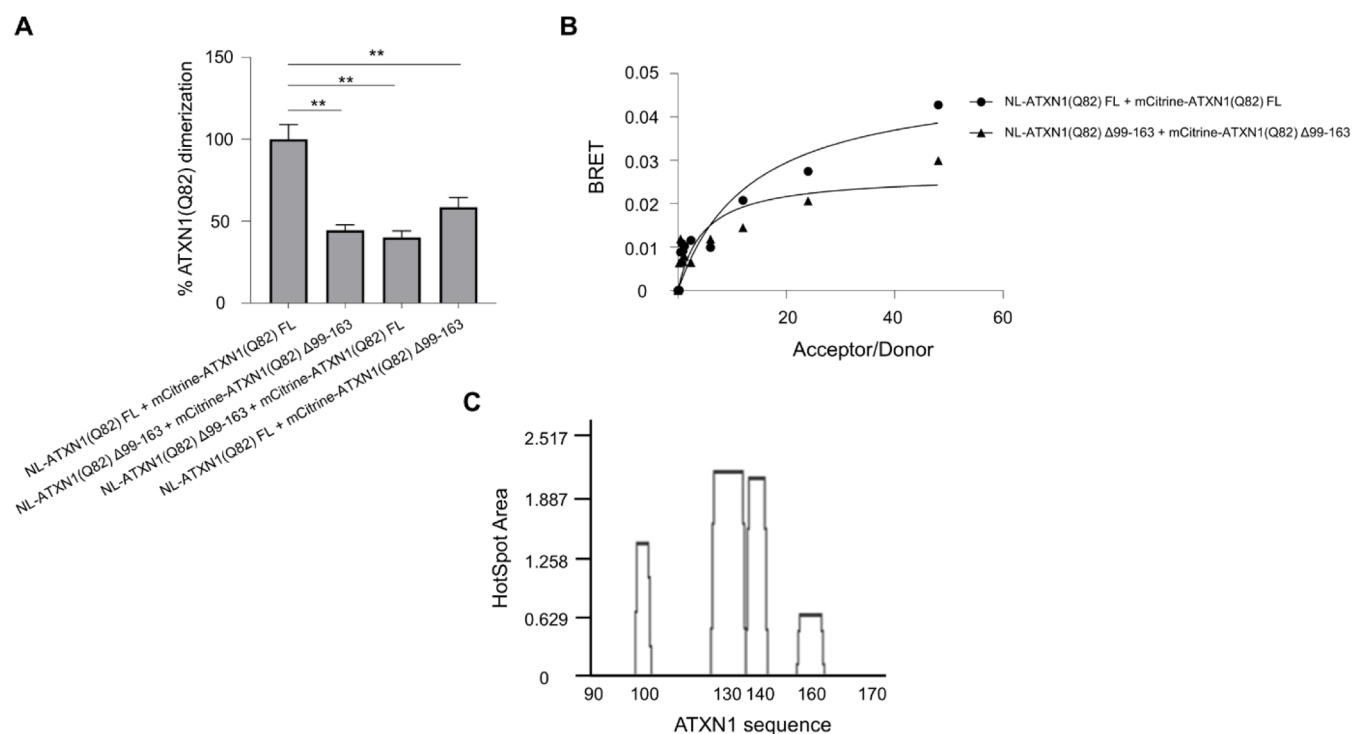


Figure 3. The aa99–163 domain is critical for the homodimerization of polyQ-expanded ATXN1. (A) Quantification of the homodimerization of full-length or $\Delta 99$ –163 ATXN1(Q82) using the LuTHy assay. The bar graph shows various combinations of full-length or deletion-carrying ATXN1 proteins. Error bars denote mean \pm SD (** $p < 0.01$). (B) Donor saturation assay indicating the effect of aa99–163 deletion in ATXN1(Q82) dimerization. (C) AGGRESCAN analysis indicating aggregation-prone regions at the N-terminal of ATXN1.

providing a reproducible readout to quantify the ATXN1-MED15 PPI (Figures 2A and S4A,B).

Then, the predicted PPI sites were individually deleted from the full-length ATXN1 and MED15 genes. In total, 5 deletion clones for ATXN1 ($\Delta 99$ –163, $\Delta 198$ –248, $\Delta 328$ –417, $\Delta 547$ –691, and $\Delta 493$ –540) and 5 deletion clones for MED15 ($\Delta 101$ –294, $\Delta 195$ –294, $\Delta 395$ –443, $\Delta 548$ –665, and $\Delta 635$ –695) were generated and subsequently shuttled into LuTHy expression plasmids. The expression efficiency of these constructs was assessed by immunoblotting in extracts from transiently transfected HEK293T cells. Distinct protein bands corresponding to the respective ATXN1 and MED15 FL and deletion clones were detected at their expected molecular weights, confirming the successful production of deletion-carrying recombinant proteins (Figure S4C,D). According to our hypothesis, deletion of the predicted PPI sites would result in a reduction or loss of the cBRET signal corresponding to the ATXN1-MED15 PPI. Therefore, PPIs between full-length ATXN1 and deletion clones of MED15 or deletion clones of ATXN1 and full-length MED15 were quantified using the LuTHy assay. Results indicated that deletion of aa99–163 or aa493–540 from ATXN1 resulted in a significant reduction of its PPI with MED15. Similarly, a reduction was observed when aa101–294, aa195–294, or aa548–665 region was deleted from MED15 (Figure S5A). To exclude false positives, LuTHy assays were repeated using combinations of hit ATXN1 and MED15 deletion clones. Notably, the simultaneous deletion of ATXN1 aa99–163 and MED15 aa548–665 resulted in a complete loss of PPI (Figure 2A). In line with the experimental data, the computational prediction of the interaction between ATXN1^{NT} aa99–163 and MED15 aa548–665 is shown in Figure 2B. These combined data suggest that the interaction

between ATXN1 and MED15 primarily occurs through this predicted PPI site.

To gain molecular-level information on the ATXN1-MED15 PPI, we performed a high-resolution docking analysis followed by MD simulations. These analyses highlighted key aa residues involved in the PPI, their interaction types, and the interatomic distances stabilizing the protein complex. Molecular docking indicated the formation of three hydrogen bonds, one salt bridge, 2 van der Waals bonds, and a Pi-Pi stacking interaction between key aa residues in ATXN1 and MED15 (Figure 2C). MD simulations also showed that these hydrogen bonds remained stable over time (Figure S5B). Structural stability of the ATXN1-MED15 PPI was further analyzed through root-mean-square deviation (RMSD) and radius of gyration (Rg) calculations, which indicate docking efficiency and distribution of atoms with respect to an axis of rotation, respectively. RMSD analysis confirmed a stable binding mode with a median RMSD of 0.12 nm and minimal deviation over time (Figure 2D and Table S2). Additionally, the Rg analysis suggested that the ATXN1-MED15 complex remained structurally compact, with no significant expansion or collapse throughout the simulation. To further assess the stability and energetics of the ATXN1-MED15 PPI, we calculated the binding free energies over a 100 ns MD simulation using the Molecular Mechanics Poisson–Boltzmann Surface Area (MM-PBSA) approach. The computed binding free energy, with a median of -10.4 kcal/mol, indicates a stable and energetically favorable interaction between ATXN1 and MED15 (Table S2).

The aa99–163 Region is Involved in ATXN1 Dimerization. Sequences flanking the polyQ region are known to influence the dimerization and aggregation of various polyQ proteins.²⁷ The aa99–163 domain of ATXN1

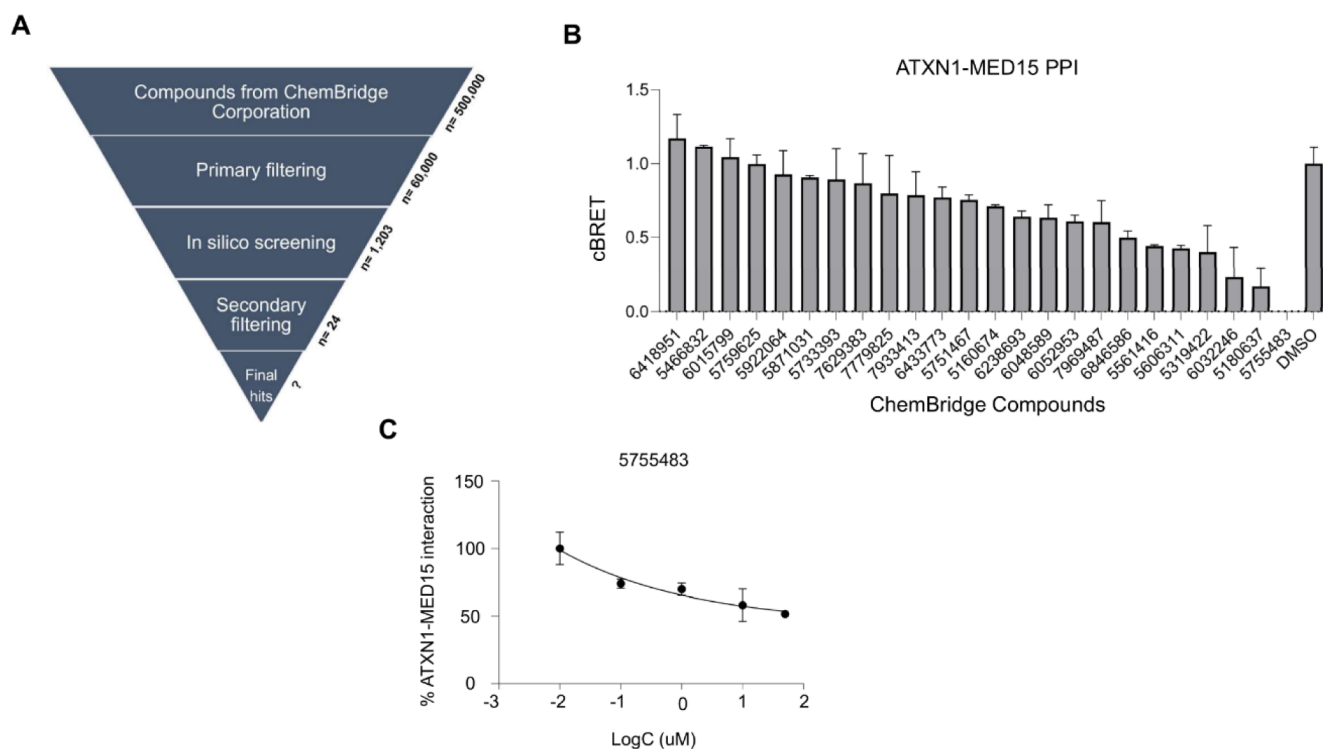


Figure 4. Screening for compounds suppressing ATXN1-MED15 PPI. (A) Workflow of AI-based virtual screening. The screening process included compounds from ChemBridge Corporation, followed by primary filtering, computational docking to ATXN1 aa99–163, and secondary filtering for the selection of predicted hits. (B) Effect of computationally predicted compounds on ATXN1-MED15 PPI using the LuTHy assay. Nine compounds significantly suppressed the interaction by at least 20% compared to the control DMSO treatment, with compound 5755483 exhibiting the strongest inhibitory effect. (C) Concentration–response curve of compound 5755483 in the ATXN1-MED15 PPI. The *x*-axis represents the log concentration of the compound, while the *y*-axis shows the percentage of ATXN1-MED15 interaction.

seems to be critical for its interaction with MED15. However, this 65-residue sequence, located upstream of the polyQ region, may also mediate ATXN1 aggregation or other PPIs, including the self-interaction/homodimerization of polyQ-expanded ATXN1. To investigate this hypothesis, we deleted this domain from both wild-type ATXN1 (Q30) and pathogenic ATXN1(Q82); then, we quantified the homodimerization of deletion-carrying ATXN1 proteins using the LuTHy assay. Analysis of the cBRET signal revealed that deletion of aa99–163 significantly suppressed the homodimerization of pathogenic ATXN1 compared to the full-length protein (Figure 3A). A similar suppression of homodimerization was also observed for ATXN1(Q30) (Figure S6), which is known to self-associate and form soluble IIBs in overexpression models.²² Donor saturation curves indicated significantly lower BRET ratios for Δ 99–163 vs FL ATXN1 (Q82) dimers, suggesting a lower homodimerization affinity for the deletion-carrying mutant isoform (Figure 3B). These data suggest that the aa99–163 domain is not only critical for ATXN1-MED15 PPI but also important for ATXN1 self-interaction.

Given that dimerization is the initial step of protein aggregation, we further assessed the aggregation propensity of ATXN1 aa99–163. A sequence-based structural analysis was performed by using the AGGRESCAN algorithm. Key parameters associated with the aggregation profile (AP) of the polypeptide, including the average aggregation-propensity values per amino acid (a4v) and the HSA (hot spot area) for each aa residue, were calculated. This computational analysis predicted an aggregation-prone aa stretch at residues 125–143 within ATXN1 aa99–163, suggesting that this domain has a

high propensity for protein aggregation (Figure 3C and Table S3).

AI-Based Virtual Screening for Compounds Binding to ATXN1 aa99–163. Since the aa99–163 domain is involved in ATXN1 interactions, we sought to identify chemical compounds that would bind to this domain and might be neuroprotective. To this end, we performed a virtual screening against this domain using the predicted ATXN1^{NT} structure, which contains at least three compound-binding pockets with high druggability probability (Table S4). First, the commercially available ChemBridge EXPRESS-Pick Stock library, comprising approximately 500,000 compounds, was downloaded and pre-filtered according to a drug-like subset of pharmacokinetic (PK) properties to exclude non-favorable compounds from the process and minimize the load. Filtering included descriptors like Lipinski's rule of 5. Furthermore, pan-assay interfering compounds (PAINS) and unwanted metabolites were removed, and the Eli Lilly MedChem set of rules, along with a favorable PPI profile, were applied. This prefiltering step resulted in a reduced set of approximately 60,000 compounds for virtual screening. The prefiltered compounds were progressed to virtual screening using an AI-assisted pipeline, which combined Smina docking results with a convolutional neural network (CNN)-based rescoring function. Our rescoring scheme assigned a low score to the majority of the screened compounds, while only a few of them were distinguished (Figure S7A). We decided to qualify as potential hits the top 2% of the solutions, corresponding to 1,203 compounds with screening scores higher than 0.901. These potential hits were further grouped into 214 clusters

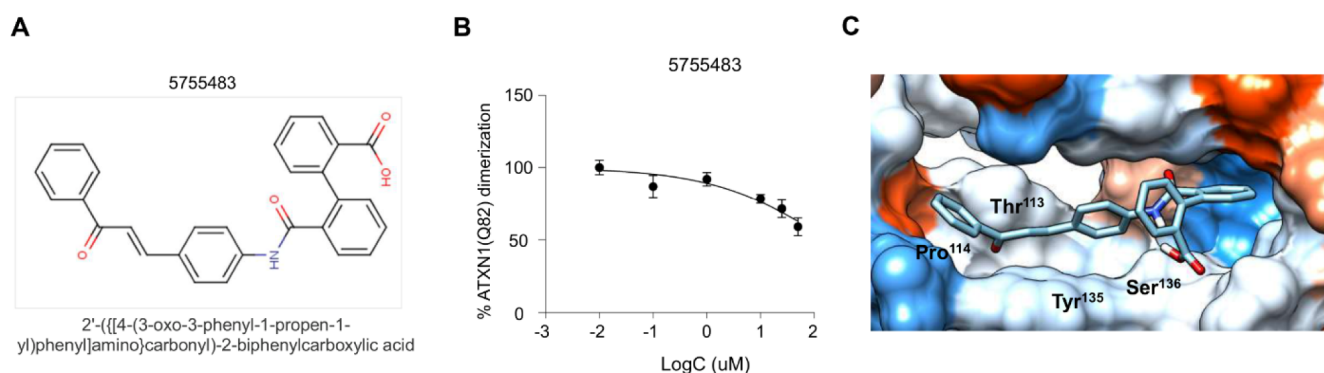


Figure 5. Compound 5755483 binds to ATXN1 and suppresses the homo-dimerization of pathogenic ATXN1. (A) Structure of Chembridge compound 5755483. (B) Dose-dependent effect of compound 5755483 in the homo-dimerization of pathogenic ATXN1. (C) Docking simulation of compound 5755483 on the aa99–163 domain of ATXN1 identified the amino acids of ATXN1 that interact with the compound through hydrogen bonding, Pi-Pi stacking, or hydrophobic interactions.

based on their structural similarity, and only one compound per cluster was selected for the next phase. This final set of compounds was subjected to a secondary post-filtering step based on molecular modeling, properties, and protein–ligand interactions. This rigorous selection process finally resulted in the identification of 24 hit compounds, which are quite diverse in structure (Figure S7B) and exhibited high binding scores to aa99–163 of ATXN1 (Table S5). A schematic overview of the complete virtual screening pipeline is shown in Figure 4A.

Compound 5755483 Binds to ATXN1 aa99–163 and Suppresses polyQ Protein Aggregation. The binding affinity of the 24 hit compounds for ATXN1 aa99–163 was evaluated in ligand-competition assays. First, we assessed their effect on ATXN1-MED15 PPI using the previously established LuTHy assay. In principle, this interaction should be less strong compared to ATXN1(Q82) homodimerization, which usually results in the formation of stable protein dimers and IIBs in cell-based overexpression assays.¹⁹ Transfected cells were treated for 48 h with the highest non-cytotoxic concentration (Figure S8) of each compound, as indicated by the MTT assay, and those that reduced ATXN1-MED15 PPI by at least 20% were considered positive hits. Based on this criterion, nine compounds (Chembridge ID: 5319422, 6433773, 5180637, 5606311, 5755483, 7969487, 6846586, 5751467, 6032246) significantly suppressed ATXN1-MED15 PPI compared to control samples treated with the solvent (DMSO). Notably, compound 5755483 (2'-([4-(3-oxo-3-phenyl-1-propen-1-yl)phenyl]amino)carbonyl)-2-biphenylcarboxylic acid) completely abolished the interaction (Figure 4B). Due to its structural characteristics, the above compound might act as a Michael acceptor, binding to several nucleophilic sites acting as PAINS. However, such compounds and unwanted metabolites were already removed, and the Eli Lilly MedChem set of rules, along with a favorable PPI profile, were applied. In order to remove any false positives, these nine compounds were further evaluated for their inhibitory effect in dose–response LuTHy assays. Indeed, six out of nine compounds tested efficiently suppressed ATXN1-MED15 PPI in a dose-dependent manner (Figures S9 and S10) with compound 5755483 demonstrating a potent effect (Figure 4C).

Finally, we investigated whether the binding of these compounds to ATXN1 aa99–163 also inhibits the dimerization of pathogenic ATXN1. Utilizing the previously established LuTHy assay for ATXN1 (Q82) dimerization, we observed

that only compound 5755483 (Figure 5A) suppressed mutant ATXN1 dimerization in a dose-dependent manner (Figure 5B). A similar effect was also observed in the dimerization of ATXN1(Q30) (Figure S6B). To assess the stability of compound 5755483 binding on ATXN1 aa99–163, we performed a 100-ns MD simulation. This analysis indicated that the compound binds stably to ATXN1, with consistent interactions observed throughout the simulation. Below, the amino acids implicated in the interactions and the types of their observed interactions are detailed. More specifically, compound 5755483 forms a hydrogen bond with Ser¹³⁶ with an interaction frequency of 85% and a mean distance of 0.30 nm (Figures 5C and S11A). Additionally, Thr¹¹³ and Pro¹¹⁴ form hydrophobic interactions with the compound, showing an interaction frequency of 65%, with mean distances of 0.2 and 0.24 nm and binding free energies of -2.5 and -2.2 kcal/mol, respectively. These strong hydrophobic interactions contribute to the stabilization of the compound. Moreover, Tyr¹³⁵ participates in a Pi-Pi stacking interaction with the compound, showing an interaction frequency of 67%, a mean distance of 0.35 nm, and a binding free energy of -4.1 kcal/mol. The Pi-Pi stacking interaction with Tyr¹³⁵ potentially enhances compound stabilization (Figure 5C and Table S6). RMSD showed that the protein-compound complex remained relatively stable, with a distance of 0.2–0.4 nm over the simulation period. Additionally, root-mean-square fluctuation (RMSF), used to measure the flexibility of amino acid residues in a protein, and Rg analysis indicate that the aa99–163 domain was less flexible in the presence of the compound, suggesting that compound binding contributes to the structural stabilization of the ATXN1 protein (Figure S11B–D). No role for methionine or cysteine amino acid (the sulfur-containing acids in a protein chain) was noticed.

DISCUSSION

The Role of PPIs in polyQ Protein Aggregation. PPIs involving polyQ-expanded proteins may play an important role in modulating their aggregation.²⁸ Many of them may promote polyQ aggregation by facilitating the assembly of misfolded proteins into larger, more stable, and insoluble structures. Conversely, other interactions may mitigate aggregation by enabling the clearance or degradation of these misfolded proteins. Therefore, chemical compounds that would modulate these PPIs hold significant potential to reduce protein aggregation and alleviate the pathological effects associated

with the presence of mutant polyQ proteins. We have previously shown that MED15 interacts with ATXN1 and significantly enhances the aggregation of the mutant isoform,¹⁹ potentially promoting the inter-molecular assembly of polyQ-expanded ATXN1 into β -sheet-rich fibrils.²⁰ Indeed, YFP-ATXN1(Q82) IIBs display a distinct morphology in the presence of MED15, suggesting that this protein may act as a linker between molecules of mutant ATXN1.

Due to the absence of experimental data, the exact structure of ATXN1 remains elusive, hampering the design of efficient antiaggregating approaches. To address this limitation, we simulated the ATXN1-MED15 PPI with the aim of identifying their interaction site. While most known interactions of ATXN1 have been mapped onto the C-terminus of the protein,^{29–31} we predicted that this PPI may be mediated by the ATXN1 aa99–163 domain, located at the N-terminus of the protein. Computational approaches provide powerful predictions of protein structures and interactions but come with potential inaccuracies in modeling.²⁶ We addressed this limitation by complementing the predictions with experimental validation. This dual approach enhances the reliability of our results and establishes a basis for the identification of critical interaction sites in polyQ-expanded ATXN1.

The aa99–163 Domain Mediates ATXN1 Homo-dimerization. Our findings suggest that the ATXN1 aa99–163 domain, upstream of the polyQ stretch, directly mediates harmful PPIs. This domain also displays a high aggregation propensity. Its deletion significantly suppressed the dimerization of pathogenic ATXN1, which may be considered the first step in polyQ protein aggregation. Collectively, these results indicate the diverse functionality of the ATXN1 aa99–163 domain, not only in mediating PPIs but also in ATXN1 homodimerization and, potentially, aggregation.

Numerous studies indicate that domains other than the polyQ stretch significantly affect protein aggregation.^{32–34} For example, the addition of a 10-residue polyP sequence at the C-terminus of a polyQ peptide alters both its conformational properties and its aggregation kinetics.³⁵ In Huntington's disease (HD), the first 17 amino acids at the N-terminus (Nt17) of huntingtin influence its biochemical properties and the stability of polyQ aggregates, ultimately affecting disease progression.^{36–38} In SCA1, the AXH domain mediates ATXN1 interaction with the transcriptional repressor CIC; disruption of the ATXN1-CIC complex ameliorates SCA1-like phenotypes in mouse models.⁵

These examples highlight that chemical targeting of domains in polyQ proteins that mediate PPIs may represent a novel therapeutic strategy. However, chemical compounds with a high affinity for ATXN1 are largely missing. Using a combination of virtual screening and experimental validation, we identified the Chembridge compound 5755483 (2'-([4-(3-oxo-3-phenyl-1-propen-1-yl)phenyl]amino)carbonyl)-2-biphenylcarboxylic acid), which binds to ATXN1 aa99–163. Of particular significance is the binding of this compound to Ser¹³⁶. Serine residues are known to participate in hydrogen bonding due to the presence of a hydroxyl group in their side chain, stabilizing protein–ligand interactions. Notably, compound 5755483 disrupted both ATXN1-MED15 PPI and the dimerization of pathogenic ATXN1. Its dual functionality highlights its value for modulating polyQ protein aggregation.

Current therapeutic interventions for SCA1 focus on modulating polyQ-expanded ATXN1 levels through the use of antisense oligonucleotides. While such approaches hold

great promise, they have significant limitations as they may have off-target effects and require invasive intrathecal administration.³⁹ Alternatively, the use of small molecules targeting domains of ATXN1 that are critical for its aggregation may confer significant advantages. Small molecule therapeutics are cost-effective, are noninvasive, can cross cell membranes to reach intracellular targets, and their biodistribution can be optimized to selectively target the desired tissue.⁴⁰ Treatment with small molecules, including compound 5755483, may overcome the limitations of existing therapeutic approaches for SCA1.

CONCLUSIONS

Together, our results indicate that the aa99–163 domain of ATXN1 mediates a protein interaction with the aggregation-enhancer MED15. The same domain is also involved in the homo-dimerization of mutant ATXN1, a critical step for polyQ protein aggregation. Chemical targeting of the ATXN1 aa99–163 with the computationally predicted ChemBridge compound 5755483 suppressed both ATXN1-MED15 PPI and polyQ-expanded ATXN1 homo-dimerization. These observations suggest that compound 5755483 may confer neuroprotection against aggregation-induced SCA1 neurodegeneration.

MATERIALS AND METHODS

Generation of Tet-On YFP-ATXN1(Q82) + mCherry-MED15 MSCs. Mesenchymal stem cells (MSCs) were cultured in Dulbecco's Modified Eagle Medium (DMEM, Biowest), supplemented with 10% fetal bovine serum (FBS, Biowest) and 1X penicillin-streptomycin (Biowest). Cells were maintained in a humidified incubator at 37 °C with 5% v/v CO₂. For the generation of Tet-On YFP-ATXN1(Q82) + mCherry-MED15 MSCs, naive MSCs were isolated and characterized, as previously described.⁴¹ MSCs were seeded at a density of 2×10^5 cells per well in a 6-well plate. Transfection was performed using Xfect reagent (Clontech) with a mixture of four plasmids such as pT2-Tet/O2-YFP-ATXN1(Q82), pT2-mCherry-MED15, pT2-TetR-neoR, and pCMV(CAT)T7-SB100 transposon plasmids at a ratio of 4:3:2:1, respectively. Transfected cells were selected at day 7 post transfection using 100 μ g/mL G418 (InvivoGen). For induction of the YFP-ATXN1(Q82) transgene, doxycycline (Dox, 2 μ g/mL, Sigma-Aldrich) was added to the culture medium. The mCherry-MED15 transgene was constitutively expressed in genetically modified MSCs.

Fluorescence Microscopy. Cells were fixed with 4% (v/v) formaldehyde (Applichem) in PBS (Biowest) for 10 min and permeabilized for 10 min with 0.1% (v/v) Triton-X 100 (Sigma-Aldrich). For nuclear staining, cells were incubated with DAPI (Biotium) for 5 min at room temperature. Cells were observed using a ZOE Fluorescent Cell Imager equipped with three fluorescence channels and an integrated digital camera (Bio-Rad).

Filter Retardation Assay. Extracts of MSCs treated in the presence or absence of Dox were mixed with an equal volume of 4% w/v sodium dodecyl sulfate (SDS) supplemented with 100 mM DTT and heated at 95 °C for 10 min. Next, the samples were diluted with 100 μ L of 0.2% w/v SDS (Applichem) and filtered through a 0.2 μ m cellulose acetate membrane (Whatman, Merck). SDS-resistant inclusions retained on the membrane were detected using the anti-

ATXN1 SA4645 antibody (1:1,000 v/v).¹⁹ The intensity of SDS-resistant inclusions was quantified using ImageJ analysis software v1.54f. Statistical analysis was performed using GraphPad Prism software, version 9 (San Diego, USA).

AggreCount. IIBs were quantified using AggreCount,⁴² an ImageJ macro developed for the unbiased analysis of protein aggregates. The macrosequence utilizes a threshold-based segmentation approach to determine the optimal threshold for each image, ensuring accurate identification of IIBs. A minimum cutoff size of 5 μm^2 was applied to include only biologically relevant IIBs, which were identified, counted, and measured for size. The analysis was conducted at single-cell resolution, with 20 cells per image analyzed across five images per experimental condition, resulting in a total of 100 cells per condition. Data compilation involved recording the number and size of IIBs in each cell, allowing for a comprehensive evaluation of their distributions and characteristics.

Immunoblotting. Cells were lysed in RIPA buffer containing protease/phosphatase inhibitors (Thermo Fisher Scientific) and benzonase (Calbiochem-Novagen). Cell extracts were analyzed by SDS-PAGE electrophoresis, followed by electrotransfer onto poly(vinylidene difluoride) (PVDF) membranes (Thermo Fisher Scientific). PVDF membranes were blocked with 5% w/v nonfat dry milk in PBST for 1 h at RT and incubated with antibodies against ATXN1 (SA4645, 1:1,000 v/v dilution),¹⁹ MED15 (H00051586-M02, Abnova, 1:1,000 v/v dilution), GAPDH (5174, Cell Signaling Technologies, 1:1,000 v/v), or β -actin (4970, Cell Signaling Technologies, 1:1,000 v/v dilution). After incubation with the appropriate secondary alkaline phosphatase-conjugated antibody, protein bands were visualized by using NBT/BCIP (AppliChem).

Prediction of 3D Protein Structures. The 3D structures of full-length ATXN1 and MED15, as well as the N-terminal (ATXN1^{NT}, aa 1–196) and C-terminal (ATXN1^{CT}, aa 229–819) truncated forms of ATXN1, located upstream and downstream of the polyQ region, respectively, were predicted using the Iterative Threading ASSEMBly Refinement (I-TASSER) software.^{24,25} The resulting 3D models were evaluated based on their C-score, which represents the estimated quality of the model. The model of each ATXN1 protein (full-length ATXN1, N-terminal or C-terminal truncated fragments) with the highest C-score was selected. For MED15, two 3D models with similar C-scores were selected for docking experiments.

Pocket Druggability Prediction. The presence and druggability of pockets were predicted using the PockDrug server with the fpocket algorithm. A ligand proximity threshold of 5.5 Å was applied to determine potential ligand-binding sites. Pockets were analyzed using a set of descriptors to evaluate their druggability potential, including volume hull, which represents the total volume of the detected pocket, and hydrophobicity (Hydrophobic Kyte), measured using the Kyte-Doolittle scale to assess the hydrophobic character of the pocket. The proportions of polar and aromatic residues were also evaluated. The druggability of each pocket was assessed by using the druggability probability score. A probability score greater than 0.5 indicates a druggable pocket.⁴³

Protein Docking Simulation. For docking experiments, the Hex software was utilized.⁴⁴ Hex is based on spherical polar Fourier (SPF) correlations to accelerate the calculation of the interaction energy between local patches of the two proteins.

This energy term comprises both surface shape and electrostatic charge, providing a comprehensive evaluation of potential binding interactions. Hex generates a number of solutions, representing docked positions of the two proteins, which are sorted based on their interaction scores. For each combination of ATXN1^{NT}, ATXN1^{CT}, and ATXN1 with the two MED15 models, approximately 20 different docking solutions were generated, sorted by their docking scores. The docking solutions comprised either specific amino acid residues or groups of residues from each protein that demonstrated potential binding interactions. To ensure robustness and specificity, single amino acids were excluded from the analysis, focusing on the interactions involving groups of amino acids. The most promising docking sites were selected based on their reproducibility across multiple docking solutions and their spatial localization within the ATXN1 and MED15 proteins. The reproducibility of docking sites was determined by assessing their frequency of occurrence in the generated docking solutions. Potential docking sites that were found in spatial proximity were grouped into larger domains. Stretches of a minimum of 30 amino acids were arbitrarily considered a protein domain.

Generation of ATXN1 and MED15 Entry Clones Lacking Interaction Sites. To generate ATXN1(Q30), ATXN1(Q82), and MED15 clones lacking interaction sites, a PCR-based approach was employed. Phosphorylated primers (Table S7) were designed to hybridize immediately after the binding sites. PCRs (25 μL volume) contained 1 ng of template DNA, 0.3 mM KAPA dNTP Mix, 0.3 μM final concentration of each phosphorylated primer, and 0.5 U of KAPA HiFi DNA polymerase in 1X KAPA HiFi GC buffer (Roche). The PCR protocol consisted of 30 cycles with the following profile: 20 s denaturation at 98 °C, 15 s annealing at 60 °C, and 2.5 min extension at 72 °C in an Eppendorf apparatus. PCR products were purified from agarose gels and recircularized using T4 DNA ligase. Ligation reactions were composed of 300 ng DNA fragment, 1 μL T4 DNA ligase (Thermo Fisher Scientific), and 1X T4 ligase buffer in a total volume of 20 μL . Following an overnight incubation at 16 °C, each ligation reaction mixture was used for the transformation of Mach1 *E. coli* cells. Transformed cells were grown on agar plates supplemented with spectinomycin for MED15 deletion clones or kanamycin for ATXN1 deletion clones. Single colonies were selected and grown in LB medium supplemented with the respective antibiotic. Finally, plasmid DNA was purified from *E. coli* cells using the NucleoSpin Plasmid Kit following the manufacturer's instructions (Macherey-Nagel) and analyzed by BsrGI (NEB) restriction digestion. Deletion clones with the expected size were subjected to further verification of their identity via DNA sequencing.

Generation of ATXN1 and MED15 Expression Clones. Full-length ATXN1 and MED15 entry clones, as well as ATXN1 and MED15 entry clones with the desired deletions of binding sites, were shuttled into pcDNA3.1-PA-mCitrine-GW or pcDNA3.1-myc-NL-GW Gateway destination vectors.²¹ Recombination was performed using LR clonase enzyme (Invitrogen). Reaction mixtures were incubated at 25 °C and used for the transformation of Mach1 *E. coli* cells. Bacteria were grown on LB agar plates supplemented with 100 $\mu\text{g}/\text{mL}$ ampicillin. Plasmid extraction was carried out using the NucleoSpin Plasmid Kit. The identity of the resulting plasmids was checked by BsrGI restriction digestion.

Cytotoxicity Assays. The cytotoxicity of the compounds was assessed by using the MTT assay. HEK293T cells were cultured in 96-well plates at a seeding density of 4×10^4 cells per well at 37 °C in a 5% v/v CO₂ atmosphere. The next day, cells were treated with various concentrations of the chemical compounds [dissolved and serially diluted in dimethyl sulfoxide (DMSO, AppliChem) with concentrations ranging from 100 to 0.1 μM] or the solvent (DMSO) alone, serving as a control. The final concentration of DMSO in the culture medium was adjusted to 1% v/v. Following an appropriate incubation period of 48 h, treated cells were exposed to 0.5 μg/mL of the MTT reagent (Applichem) and further incubated for 4 h. Then, the MTT-containing medium was removed, and the formazan crystals formed by viable cells were dissolved using DMSO. To quantify cell viability, the optical density (OD) of the formazan solution was measured at two wavelengths, 570 and 630 nm, using a SPARK plate reader (Tecan).

LuThy Assay. PA-mCitrine-ATXN1/NL-MED15 were coexpressed in HEK293 cells (4×10^4 cells per well). To assess the interaction between ATXN1 and MED15, BRET/cBRET signals were quantified 48 h post transfection. Luminescence emission was measured at short (370–480 nm) and long (520–570 nm) wavelengths after the addition of the appropriate substrate. For accurate analysis and correction of donor luminescence bleed-through, BRET measurements of the positive control PA-mCitrine-NL and the negative control PA-NL were performed. The LuThy assay²¹ was then performed for the quantification of PPIs between ATXN1 and deletion clones of MED15 or the opposite combination (full-length MED15 and deletion clones of ATXN1). Luminescence measurements were used to quantify the interaction between full-length or deletion clones of ATXN1 and MED15. Protein production was estimated by total luminescence and fluorescence measurements. For donor saturation experiments, 0.5 ng of plasmid DNA encoding NL fusion proteins was cotransfected with increasing amounts (0.1–20 ng) of plasmid DNA encoding PA-mCit-tagged constructs. Measurements were performed 42 h post transfection, and BRET ratios were determined to quantify interaction strength and efficiency. LuThy assays were also performed in the presence of chemical compounds at various noncytotoxic concentrations (8–48 h treatment). To ensure specificity and accuracy of the measurements, the nonspecific/autofluorescence signal of each compound was calculated and subtracted from all relevant interactions. The percentage inhibitory effect of the compounds was then calculated by comparing the normalized cBRET signal of the treated cells to the solvent-treated control samples.

Pre-filtering and Profiling of Compounds. The ChemBridge library, comprising 500,000 molecules in SDF-formatted files, was downloaded from the Hit2Lead website (www.hit2lead.com). Prior to further analysis, this library was annotated to remove any present salts' counterions. This step was executed using OpenBabel v2.4.1.⁴⁵ Next, the library was submitted to the FAF-Drugs4 server⁴⁶ for stringent filtering based on drug-like properties, promiscuity, and PPI considerations, employing a range of ADME-Tox descriptors such as XLOGP3, PKs, bioavailability and adhering to Lilly Medchem relaxed rules.⁴⁷ Compounds meeting all filtering criteria were compiled into SDF-formatted files, forming the basis for subsequent virtual screening analyses.

AI-Based Virtual Screening. Following the prefiltering stage, accepted molecules in SDF format were subjected to virtual screening. The virtual screening pipeline integrates a novel AI-based technique, where the docking outcome of Smina⁴⁸ is combined with an AI-driven rescoring function.⁴⁹ This approach enhances the discernment of potential binding complexes with higher efficiency. Docking was performed on two different compound conformations, resulting in 50 (50) docked poses per molecule conformation. The resulting protein-compound docked complexes were rescored using our custom AI-based rescoring function, a 3D neural network (3D-CNN), which has previously been shown to outperform Smina in more effectively quantifying the protein–ligand binding mechanism.⁴⁹ The top-scoring molecules were further categorized into clusters based on their structural similarity, utilizing a 3D shape descriptor,⁵⁰ and one molecule per cluster was finally qualified for further processing.⁵¹

Post-filtering of Compounds. The remaining compounds were post-filtered based on three key criteria: molecular modeling, molecular properties, and the nature of protein–ligand interactions formed during docking simulations. This strategy ensured a rigorous evaluation process encompassing both structural and functional aspects of the protein–ligand complexes.

Molecular Dynamics. Molecular dynamics (MD) simulations of protein–protein complexes and protein-inhibitor systems were performed using GROMACS 2024.4.⁵² The CHARMM36 force field was used for all simulations. The system was resolved using a 1 nm dodecahedron water box, with chloride ions added to generate a charge-neutral system. The system was first minimized, followed by temperature and pressure equilibration under an NVT ensemble for 100 ps and then an NPT ensemble for an additional 100 ps. MD simulations were performed for 100 ns for each system at 300 K. Analysis of molecular dynamics was performed using GROMACS utilities and scripts in the Python environment.

Prediction of Aggregation Propensity. The aggregation propensity of the ATXN1(Q82) protein was analyzed using the AGGRESCAN algorithm.⁵³ The peptide sequence of ATXN1(Q82) was submitted to the AGGRESCAN server in FASTA format. Aggregation propensities of amino acids were calculated by using the default settings. Key parameters, such as the average aggregation-propensity values per amino acid (a4v) and the HSA (hot spot area) for each amino acid residue, were calculated.

Statistics and Data Fitting. All experimental assays were conducted in technical triplicate to ensure robustness and reproducibility of the results. The data are expressed as the mean ± standard deviation. To assess the potency of inhibitory compounds, the half-maximal inhibitory concentration (IC₅₀) values were determined. Inhibition data were converted to % inhibition and fitted using a standard log inhibitor vs normalized response model through nonlinear regression analysis in GraphPad Prism software version 9.0.0 (Boston, Massachusetts USA). This fitting process allowed for the accurate determination of IC₅₀ values, providing crucial insights into the compound's efficacy in modulating the targeted interactions or dimerization events.

■ ASSOCIATED CONTENT

Supporting Information

The Supporting Information is available free of charge at <https://pubs.acs.org/doi/10.1021/acsomega.5c02465>.

Tables S1–S7 containing information on computational analyses of protein and compound dockings, virtual screening, MD simulations and pocket detection in target proteins. Figures S1–S11 presenting complementary experimental and computational results on the effect of chemical compounds in cell models utilized in this study (PDF)

AUTHOR INFORMATION

Corresponding Author

Spyros Petrakis – Institute of Applied Biosciences, Centre for Research and Technology Hellas, Thessaloniki 57001, Greece; orcid.org/0000-0001-9094-3480; Email: spetrak@certh.gr

Authors

Ioannis Gkekas – Institute of Applied Biosciences, Centre for Research and Technology Hellas, Thessaloniki 57001, Greece; Laboratory of Pharmacology, School of Pharmacy, Faculty of Health Sciences, Aristotle University of Thessaloniki, Thessaloniki 54124, Greece; orcid.org/0009-0006-7840-6344

Katerina Pliatsika – Institute of Applied Biosciences, Centre for Research and Technology Hellas, Thessaloniki 57001, Greece; Laboratory of Pharmacology, School of Pharmacy, Faculty of Health Sciences, Aristotle University of Thessaloniki, Thessaloniki 54124, Greece; orcid.org/0009-0000-1106-3435

Stelios Mylonas – Information Technologies Institute, Centre for Research and Technology Hellas, Thessaloniki 57001, Greece

Sotirios Katsamakos – Laboratory of Pharmaceutical Chemistry, School of Pharmacy, Faculty of Health Sciences, Aristotle University of Thessaloniki, Thessaloniki 54124, Greece

Apostolos Axenopoulos – Information Technologies Institute, Centre for Research and Technology Hellas, Thessaloniki 57001, Greece

Simona Kostova – Max-Delbrueck-Center for Molecular Medicine in the Helmholtz Association, Berlin 13125, Germany

Erich E. Wanker – Max-Delbrueck-Center for Molecular Medicine in the Helmholtz Association, Berlin 13125, Germany

Dimitra Hadjipavlou-Litina – Laboratory of Pharmaceutical Chemistry, School of Pharmacy, Faculty of Health Sciences, Aristotle University of Thessaloniki, Thessaloniki 54124, Greece

Konstantinos Xanthopoulos – Institute of Applied Biosciences, Centre for Research and Technology Hellas, Thessaloniki 57001, Greece; Laboratory of Pharmacology, School of Pharmacy, Faculty of Health Sciences, Aristotle University of Thessaloniki, Thessaloniki 54124, Greece

Petros Daras – Information Technologies Institute, Centre for Research and Technology Hellas, Thessaloniki 57001, Greece; orcid.org/0000-0003-3814-6710

Complete contact information is available at: <https://pubs.acs.org/10.1021/acsomega.5c02465>

Author Contributions

#I.G. and K.P. contributed equally. The manuscript was written through the contributions of all authors. All authors have given approval to the final version of the manuscript.

Funding

The open access publishing of this article is financially supported by HEAL-Link.

Notes

The authors declare no competing financial interest.

ACKNOWLEDGMENTS

The authors wish to thank Zsuzsanna Izsvák and Zoltán Ivics for kindly providing components of the SB100X transposon system and Sigrid Schnögl for carefully reading the manuscript. This study was supported by: 1) the Hellenic Foundation for Research and Innovation (HFRI) and the General Secretariat for Research and Innovation (GSRI) under the 1st Call for research projects to support Postdoctoral Researchers (Grant Agreement No. 122) and 2) the HFRI under the 3rd Call for HFRI PhD Fellowships (Fellowship Number: 6654).

ABBREVIATIONS

aa, amino acids; ATXN1, ataxin-1; cc, coiled-coil; CT, C-terminal; CNN, convolutional neural network; FL, full-length; IIBs, intranuclear inclusion bodies; MD, molecular dynamics; NT, N-terminal; Rg, radius of gyration; RMSD, root-mean-square deviation; RMSF, root-mean-square fluctuation; polyQ, polyglutamine; SCA1, spinocerebellar ataxia type 1

REFERENCES

- (1) Orr, H. T.; Zoghbi, H. Y. SCA1Molecular Genetics: A History of a 13 Year Collaboration against Glutamines. *Hum. Mol. Genet.* **2001**, *10* (20), 2307–2311.
- (2) Orr, H. T.; Chung, M.; Banfi, S.; Kwiatkowski, T. J.; Servadio, A.; Beaudet, A. L.; McCall, A. E.; Duvick, L. A.; Ranum, L. P. W.; Zoghbi, H. Y. Expansion of an Unstable Trinucleotide CAG Repeat in Spinocerebellar Ataxia Type 1. *Nat. Genet.* **1993**, *4* (3), 221–226.
- (3) Koeppe, A. The Pathogenesis of Spinocerebellar Ataxia. *Cerebellum* **2005**, *4* (1), 62–73.
- (4) Handler, H. P.; Duvick, L.; Mitchell, J. S.; Cvetanovic, M.; Reighard, M.; Soles, A.; Mather, K. B.; Rainwater, O.; Serres, S.; Nichols-Meade, T.; et al. Decreasing Mutant ATXN1 Nuclear Localization Improves a Spectrum of SCA1-like Phenotypes and Brain Region Transcriptomic Profiles. *Neuron* **2023**, *111* (4), 493–507.e6.
- (5) Coffin, S. L.; Durham, M. A.; Nitschke, L.; Xhako, E.; Brown, A. M.; Revelli, J.-P.; Villavicencio Gonzalez, E.; Lin, T.; Handler, H. P.; Dai, Y.; et al. Disruption of the ATXN1-CIC Complex Reveals the Role of Additional Nuclear ATXN1 Interactors in Spinocerebellar Ataxia Type 1. *Neuron* **2023**, *111* (4), 481–492.e8.
- (6) Servadio, A.; Koshy, B.; Armstrong, D.; Antalffy, B.; Orr, H. T.; Zoghbi, H. Y. Expression Analysis of the Ataxin-1 Protein in Tissues from Normal and Spinocerebellar Ataxia Type 1 Individuals. *Nat. Genet.* **1995**, *10* (1), 94–98.
- (7) Kang, S.; Hong, S. Molecular Pathogenesis of Spinocerebellar Ataxia Type 1 Disease. *Mol. Cells* **2009**, *27* (6), 621–627.
- (8) Burchette, E. Identification of a Self-Association Region within the SCA1 Gene Product, Ataxin-1. *Hum. Mol. Genet.* **1997**, *6* (4), 513–518.
- (9) de Chiara, C.; Menon, R. P.; Dal Piaz, F.; Calder, L.; Pastore, A. Polyglutamine Is Not All: The Functional Role of the AXH Domain in the Ataxin-1 Protein. *J. Mol. Biol.* **2005**, *354* (4), 883–893.
- (10) Klement, I. A.; Skinner, P. J.; Kaytor, M. D.; Yi, H.; Hersch, S. M.; Clark, H. B.; Zoghbi, H. Y.; Orr, H. T. Ataxin-1 Nuclear

Localization and Aggregation: Role in Polyglutamine-Induced Disease in SCA1 Transgenic Mice. *Cell* **1998**, *95* (1), 41–53.

(11) Bolger, T. A.; Zhao, X.; Cohen, T. J.; Tsai, C.-C.; Yao, T.-P. The Neurodegenerative Disease Protein Ataxin-1 Antagonizes the Neuronal Survival Function of Myocyte Enhancer Factor-2. *J. Biol. Chem.* **2007**, *282* (40), 29186–29192.

(12) Cvetanovic, M.; Rooney, R. J.; Garcia, J. J.; Toporovskaya, N.; Zoghbi, H. Y.; Opal, P. The Role of LANP and Ataxin 1 in E4F-Mediated Transcriptional Repression. *EMBO Rep.* **2007**, *8* (7), 671–677.

(13) Goold, R.; Hubank, M.; Hunt, A.; Holton, J.; Menon, R. P.; Revesz, T.; Pandolfo, M.; Matilla-Duenas, A. Down-Regulation of the Dopamine Receptor D2 in Mice Lacking Ataxin 1. *Hum. Mol. Genet.* **2007**, *16* (17), 2122–2134.

(14) Okazawa, H.; Rich, T.; Chang, A.; Lin, X.; Waragai, M.; Kajikawa, M.; Enokido, Y.; Komuro, A.; Kato, S.; Shibata, M.; Hatanaka, H.; Mouradian, M. M.; Sudol, M.; Kanazawa, I. Interaction between Mutant Ataxin-1 and PQBP-1 Affects Transcription and Cell Death. *Neuron* **2002**, *34* (5), 701–713.

(15) Serra, H. G.; Duvick, L.; Zu, T.; Carlson, K.; Stevens, S.; Jorgensen, N.; Lysholm, A.; Burrell, E.; Zoghbi, H. Y.; Clark, H. B.; Andresen, J. M.; Orr, H. T. ROR α -Mediated Purkinje Cell Development Determines Disease Severity in Adult SCA1 Mice. *Cell* **2006**, *127* (4), 697–708.

(16) Lam, Y. C.; Bowman, A. B.; Jafar-Nejad, P.; Lim, J.; Richman, R.; Fryer, J. D.; Hyun, E. D.; Duvick, L. A.; Orr, H. T.; Botas, J.; Zoghbi, H. Y. ATAXIN-1 Interacts with the Repressor Capicua in Its Native Complex to Cause SCA1 Neuropathology. *Cell* **2006**, *127* (7), 1335–1347.

(17) Rousseaux, M. W. C.; Tschumperlin, T.; Lu, H.-C.; Lackey, E. P.; Bondar, V. V.; Wan, Y.-W.; Tan, Q.; Adamski, C. J.; Friedrich, J.; Twaroski, K.; et al. ATXN1-C1C Complex Is the Primary Driver of Cerebellar Pathology in Spinocerebellar Ataxia Type 1 through a Gain-of-Function Mechanism. *Neuron* **2018**, *97* (6), 1235–1243.e5.

(18) Cooper, D. G.; Fassler, J. S. Med15: Glutamine-Rich Mediator Subunit with Potential for Plasticity. *Trends Biochem. Sci.* **2019**, *44* (9), 737–751.

(19) Petrakis, S.; Raskó, T.; Russ, J.; Friedrich, R. P.; Stroedicke, M.; Riechers, S.-P.; Muehlenberg, K.; Möller, A.; Reinhardt, A.; Vinayagam, A.; Schaefer, M. H.; Boutros, M.; Tricoire, H.; Andrade-Navarro, M. A.; Wanker, E. E. Identification of Human Proteins That Modify Misfolding and Proteotoxicity of Pathogenic Ataxin-1. *PLoS Genet.* **2012**, *8* (8), No. e1002897.

(20) Petrakis, S.; Schaefer, M. H.; Wanker, E. E.; Andrade-Navarro, M. A. Aggregation of PolyQ-extended Proteins Is Promoted by Interaction with Their Natural Coiled-coil Partners. *BioEssays* **2013**, *35* (6), 503–507.

(21) Trepte, P.; Kruse, S.; Kostova, S.; Hoffmann, S.; Buntru, A.; Tempelmeier, A.; Secker, C.; Diez, L.; Schulz, A.; Klockmeier, K.; et al. LuTHy: A Double-readout Bioluminescence-based Two-hybrid Technology for Quantitative Mapping of Protein–Protein Interactions in Mammalian Cells. *Mol. Syst. Biol.* **2018**, *14* (7), No. e8071.

(22) Laidou, S.; Alanis-Lobato, G.; Příbyl, J.; Raskó, T.; Tichy, B.; Mikulasek, K.; Tsagiopoulou, M.; Oppelt, J.; Kastrinaki, G.; Lefaki, M.; Singh, M.; Zink, A.; Chondrogianni, N.; Psoomopoulos, F.; Prigione, A.; Ivics, Z.; Pospisilova, S.; Skladal, P.; Izsvák, Z.; Andrade-Navarro, M. A.; Petrakis, S. Nuclear Inclusions of Pathogenic Ataxin-1 Induce Oxidative Stress and Perturb the Protein Synthesis Machinery. *Redox Biol.* **2020**, *32*, 101458.

(23) Kawooya, J. K.; Emmons, T. L.; Gonzalez-DeWhitt, P. A.; Camp, M. C.; D'Andrea, S. C. Electrophoretic Mobility of Alzheimer's Amyloid- β Peptides in Urea–Sodium Dodecyl Sulfate–Polyacrylamide Gel Electrophoresis. *Anal. Biochem.* **2003**, *323* (1), 103–113.

(24) Zhang, Y. I-TASSER Server for Protein 3D Structure Prediction. *BMC Bioinf.* **2008**, *9* (1), 40.

(25) Yang, J.; Zhang, Y. Protein Structure and Function Prediction Using I-TASSER. *Curr. Protoc. Bioinf.* **2015**, *52* (1), 5–8.

(26) Truant, R.; Harding, R. J.; Neuman, K.; Maiuri, T. Revisiting Huntingtin Activity and Localization Signals in the Context of Protein Structure. *J. Huntingtons Dis.* **2024**, *13* (4), 419–430.

(27) Saunders, H. M.; Bottomley, S. P. Multi-domain misfolding: Understanding the Aggregation Pathway of Polyglutamine Proteins. *Protein Eng., Des. Sel.* **2009**, *22* (8), 447–451.

(28) Vagiona, A.-C.; Notopoulou, S.; Zdráhal, Z.; Gonçalves-Kulik, M.; Petrakis, S.; Andrade-Navarro, M. A. Prediction of Protein Interactions with Function in Protein (de-)Phosphorylation. *PLoS One* **2025**, *20* (3), No. e0319084.

(29) Tejwani, L.; Lim, J. Pathogenic Mechanisms Underlying Spinocerebellar Ataxia Type 1. *Cell. Mol. Life Sci.* **2020**, *77* (20), 4015–4029.

(30) Pérez Ortiz, J. M.; Orr, H. T. Spinocerebellar Ataxia Type 1: Molecular Mechanisms of Neurodegeneration and Preclinical Studies. *Polyglutamine Disorders*. Springer, 2018; 135–145.

(31) Ju, H.; Kokubu, H.; Lim, J. Beyond the Glutamine Expansion: Influence of Posttranslational Modifications of Ataxin-1 in the Pathogenesis of Spinocerebellar Ataxia Type 1. *Mol. Neurobiol.* **2014**, *50* (3), 866–874.

(32) Nozaki, K.; Onodera, O.; Takano, H.; Tsuji, S. Amino Acid Sequences Flanking Polyglutamine Stretches Influence Their Potential for Aggregate Formation. *Neuroreport* **2001**, *12* (15), 3357–3364.

(33) Menon, R. P.; Pastore, A. Expansion of Amino Acid Homosequences in Proteins: Insights into the Role of Amino Acid Homopolymers and of the Protein Context in Aggregation. *Cell. Mol. Life Sci.* **2006**, *63* (14), 1677–1685.

(34) Kuiper, E. F. E.; de Mattos, E. P.; Jardim, L. B.; Kampinga, H. H.; Bergink, S. Chaperones in Polyglutamine Aggregation: Beyond the Q-Stretch. *Front. Neurosci.* **2017**, *11*, 145.

(35) Bhattacharyya, A.; Thakur, A. K.; Chellgren, V. M.; Thiagarajan, G.; Williams, A. D.; Chellgren, B. W.; Creamer, T. P.; Wetzel, R. Oligoproline Effects on Polyglutamine Conformation and Aggregation. *J. Mol. Biol.* **2006**, *355* (3), 524–535.

(36) Crick, S. L.; Ruff, K. M.; Garai, K.; Frieden, C.; Pappu, R. V. Unmasking the Roles of N- and C-Terminal Flanking Sequences from Exon 1 of Huntingtin as Modulators of Polyglutamine Aggregation. *Proc. Natl. Acad. Sci. U. S. A.* **2013**, *110* (50), 20075–20080.

(37) Sahoo, B.; Singer, D.; Kodali, R.; Zuchner, T.; Wetzel, R. Aggregation Behavior of Chemically Synthesized, Full-Length Huntingtin Exon1. *Biochemistry* **2014**, *53* (24), 3897–3907.

(38) Vieweg, S.; Mahul-Mellier, A.-L.; Ruggeri, F. S.; Riguet, N.; DeGuire, S. M.; Chiki, A.; Cendrowska, U.; Dietler, G.; Lashuel, H. A. The Nt17 Domain and Its Helical Conformation Regulate the Aggregation, Cellular Properties and Neurotoxicity of Mutant Huntingtin Exon 1. *J. Mol. Biol.* **2021**, *433* (21), 167222.

(39) Lauffer, M. C.; van roon-Mom, W.; Aartsma-Rus, A. Possibilities and Limitations of Antisense Oligonucleotide Therapies for the Treatment of Monogenic Disorders. *Commun. Med.* **2024**, *4* (1), 6.

(40) Southey, M. W. Y.; Brunavs, M. Introduction to Small Molecule Drug Discovery and Preclinical Development. *Front. Drug Discovery* **2023**, *3*, 3.

(41) Siska, E. K.; Weisman, I.; Romano, J.; Ivics, Z.; Izsvák, Z.; Barkai, U.; Petrakis, S.; Koliakos, G. Generation of an Immortalized Mesenchymal Stem Cell Line Producing a Secreted Biosensor Protein for Glucose Monitoring. *PLoS One* **2017**, *12* (9), No. e0185498.

(42) Klickstein, J. A.; Mukkavalli, S.; Raman, M. AggreCount: An Unbiased Image Analysis Tool for Identifying and Quantifying Cellular Aggregates in a Spatially Defined Manner. *J. Biol. Chem.* **2020**, *295* (51), 17672–17683.

(43) Hussein, H. A.; Borrel, A.; Geneix, C.; Petitjean, M.; Regad, L.; Camproux, A.-C. PockDrug-Server: A New Web Server for Predicting Pocket Druggability on Holo and Apo Proteins. *Nucleic Acids Res.* **2015**, *43* (W1), W436–W442.

(44) Ritchie, D. W.; Kemp, G. J. Protein Docking Using Spherical Polar Fourier Correlations. *Proteins: Struct., Funct., Bioinf* **2000**, *39* (2), 178–194.

- (45) O'Boyle, N. M.; Banck, M.; James, C. A.; Morley, C.; Vandermeersch, T.; Hutchison, G. R. Open Babel: An Open Chemical Toolbox. *J. Cheminf.* **2011**, *3* (1), 33.
- (46) Lagorce, D.; Bousslama, L.; Becot, J.; Miteva, M. A.; Villoutreix, B. O. FAF-Drugs4: Free ADME-Tox Filtering Computations for Chemical Biology and Early Stages Drug Discovery. *Bioinformatics* **2017**, *33* (22), 3658–3660.
- (47) Mannhold, R.; Poda, G. I.; Ostermann, C.; Tetko, I. V. Calculation of Molecular Lipophilicity: State-of-the-Art and Comparison of LogP Methods on More than 96,000 Compounds. *J. Pharm. Sci.* **2009**, *98* (3), 861–893.
- (48) Koes, D. R.; Baumgartner, M. P.; Camacho, C. J. Lessons Learned in Empirical Scoring with Smina from the CSAR 2011 Benchmarking Exercise. *J. Chem. Inf. Model.* **2013**, *53* (8), 1893–1904.
- (49) Mylonas, S.; Axenopoulos, A.; Katsamakas, S.; Gkekas, I.; Stamatopoulos, K.; Petrakis, S.; Daras, P. Deep Learning-Assisted Pipeline for Virtual Screening of Ligand Compound Databases: Application on Inhibiting the Entry of SARS-CoV-2 into Human Cells. In *2020 IEEE 20th International Conference on Bioinformatics and Bioengineering (BIBE)*; IEEE, 2020; pp 132–139. .
- (50) Axenopoulos, A.; Rafailidis, D.; Papadopoulos, G.; Houstis, E. N.; Daras, P. Similarity Search of Flexible 3D Molecules Combining Local and Global Shape Descriptors. *IEEE/ACM Trans. Comput. Biol. Bioinf.* **2016**, *13* (5), 954–970.
- (51) Gkekas, I.; Katsamakas, S.; Mylonas, S.; Fotopoulou, T.; Magoulas, G. E.; Tenchiu, A. C.; Dimitriou, M.; Axenopoulos, A.; Rossopoulou, N.; Kostova, S.; Wanker, E. E.; Katsila, T.; Papahatjis, D.; Gorgoulis, V. G.; Koufaki, M.; Karakasiliotis, I.; Calogeropoulou, T.; Daras, P.; Petrakis, S. AI Promoted Virtual Screening, Structure-Based Hit Optimization, and Synthesis of Novel COVID-19 S-RBD Domain Inhibitors. *J. Chem. Inf. Model.* **2024**, *64* (22), 8562–8585.
- (52) Abraham, M. J.; Murtola, T.; Schulz, R.; Páll, S.; Smith, J. C.; Hess, B.; Lindahl, E. GROMACS: High Performance Molecular Simulations through Multi-Level Parallelism from Laptops to Supercomputers. *SoftwareX* **2015**, *1–2*, 19–25.
- (53) Conchillo-Solé, O.; de Groot, N. S.; Avilés, F. X.; Vendrell, J.; Daura, X.; Ventura, S. AGGRESKAN: A Server for the Prediction and Evaluation of “Hot Spots” of Aggregation in Polypeptides. *BMC Bioinf.* **2007**, *8* (1), 65.